Nicolas Binder[1]
ISAE-SUPAERO,
Université de Toulouse,
10, avenue Edouard Belin,
BP 54032,
Toulouse Cedex 4 31055, France
e-mail: nicolas.binder@isae.fr

Suk-Kee Courty-Audren
SAFRAN-TECHNOFAN,
10, place Marcel Dassault,
BP 30053,
Blagnac Cedex 31702, France

Sebastien Duplaa
ISAE-SUPAERO,
Université de Toulouse,
10, avenue Edouard Belin,
BP 54032,
Toulouse Cedex 4 31055, France

Guillaume Dufour
ISAE-SUPAERO,
Université de Toulouse,
10, avenue Edouard Belin,
BP 54032,
Toulouse Cedex 4 31055, France

Xavier Carbonneau
ISAE-SUPAERO,
Université de Toulouse,
10, avenue Edouard Belin,
BP 54032,
Toulouse Cedex 4 31055, France

Theoretical Analysis of the Aerodynamics of Low-Speed Fans in Free and Load-Controlled Windmilling Operation

The present work is a contribution to understanding the windmilling operation of low-speed fans. Such an operating situation is described in the literature, but the context (mainly windmilling of aero-engines) often involves system dependence in the analysis. Most of the time, only regimes very close to the free-windmilling are considered. A wider range is analyzed in the present study, since the context is the examination of the energy recovery potential of fans. It aims at detailing the isolated contribution of the rotor, which is the only element exchanging energy with the flow. Other elements of the system (including the stator) can be considered as loss generators and be treated as such in an integrated approach. The evolution of the flow is described by the use of theoretical and experimental data. A theoretical model is derived to predict the operating trajectories of the rotor in two characteristic diagrams. A scenario is proposed, detailing the local evolution of the flow when a gradual progression toward free and load-controlled windmilling operation is imposed. An experimental campaign exerted on two low-speed fans aims at the analysis of both the local and global aspects of the performance, for validation. From a global point of view, the continuity of the operating trajectory is predicted and observed across the boundary between the quadrants of the diagrams. The flow coefficient value for the free-windmilling operation is fairly well predicted. From a local point of view, the local co-existence of compressor and turbine operating modes along the blade span is observed as previously reported. It is further demonstrated here that this configuration is not exclusive to free-windmilling operation and occurs inside a range that can be theoretically predicted. It is shown that for a given geometry, this local topology strongly depends on the value of the flow coefficient and is very sensitive to the inlet spanwise velocity distribution. [DOI: 10.1115/1.4030308]

1 Introduction

The windmilling of fans is usually analyzed in the context of in-flight shut-off of turbofans (see Refs. [1,2] for instance). In that case, determination of the windmilling rotational speed of the fan can be critical in sizing the shaft bearing lubrication systems and the supporting structure of the engine [3]. Furthermore, the assessment of the relight capability of the engine requires the evaluation of the mass flow rate, pressure, and temperature in the combustor. Finally, the engine drag at windmill is required for integration issues. This system-dependant problematic is usually tackled through a global approach [4–6].

Regarding the local aerodynamics of the fan stage, the available experimental or numerical studies [7–9] indicate that, in the windmilling regime, the fan stage operates in a mixed fashion: the inboard sections operate in compressor-mode, while the outboard sections operate in turbine-mode. The work exchanged in the two zones cancel out, as the load on the shaft is considered negligible in that case: this is the free-windmilling regime.

However, the windmilling operation of fans is not limited to turbo-engines: with the development of a more-electrical aircraft (see Ref. [10]), some cooling fans, which are required for ground operation but normally not used during flight, are now considered as possible energy generation devices. The fan has thus to operate in a turbine-like mode, with a significant resistive load on the shaft, which can be considered as a load-controlled windmilling regime.

In the literature, very limited attention has been paid to the load-controlled windmilling regime. The first study dealing with this regime is of Turner and Sparkes [11], where all the possible combinations of inverted rotational speed, nonconventional flow direction, and shaft loading were experimented on a stator–rotor–stator stage. The same approach is developed in Refs. [12,13,14] involving both experimental and numerical methodologies for a multistage axial-flow compressor. In those studies, the relevance of the use of flow-coefficient diagrams is detailed, and a clear convention for the four-quadrant operation is proposed. However, fundamental understanding of the link between the global performance and the local flow topology remains to be achieved.

In this context, the problematic of the present study is to adopt a component-based approach focusing on load-controlled windmilling. As the target application is energy recovery, the work exchange is the quantity of interest, and therefore it is legitimate to restrict the present study to the rotor, since it is the only element that actually exchanges energy with the flow. The stator, though its demonstrated importance on the overall performance [5] can be considered as a loss generator and be subsequently treated as such. A theoretical approach is proposed, aiming at a unified and generic description of the different windmilling situations of the fan rotor. Such an approach does not aim at the accurate

prediction of the performance. The first objective is rather to construct a reference flow pattern that contains a dominant part of the physics involved. Some generic analysis is then possible, without the bias of the context imposed by the system. The second objective is to establish a link between the global performance and the local topology, in order to predict the trends when the load is varied. Those trends give a theoretical background for the assessment of the potential of conventional fans for energy recovery. Those trends are also implementable inside a system loop to achieve overall system prediction.

The present paper is decomposed into five sections. Following this introduction, the derivation of the theoretical model and the generic analysis are presented in Sec. 2. The experimental approach developed for validation is detailed in Sec. 3. The results are presented and discussed in Sec. 4. Section 5 proposes an outlook of possible applications.

2 Theoretical Model and Generic Analysis

2.1 Load-Controlled Windmilling. The literature provides a general classification of the windmilling operation (see Ref. [15]). It depends on the sign of the total pressure and total temperature variations across the stage. A positive sign for both variations characterizes the usual compressor functioning. If the loading coefficient is low enough, the work input ($\Delta T_i > 0$) may not compensate the losses ($\Delta P_i < 0$) and the fan operates in the stirrer situation. And finally, when the direction of the work exchange is inverted ($\Delta T_i < 0$ and $\Delta P_i < 0$), the fan operates in the turbine operating-mode. At the boundary between the stirrer and the turbine is found the so-called free-windmilling operating mode. The locked-rotor functioning represents the far end of the turbine functioning. For the free-windmilling (freewheeling) mode, the work extracted is considered zero because the resistive torque on the shaft is negligible. For the locked-rotor operation, the work is obviously zero as the rotational speed is null. Between these two limits, a load-controlled windmilling operation can be imposed. If the resistive torque of the shaft is correctly set, some energy recovery is possible [16].

2.2 Loading-to-Flow-Coefficient Diagrams. Loading-to-flow-coefficient diagrams are used in the literature to represent the complete performance map of fans [17]. The representation is indeed relevant, for simple relations exist between those two non-dimensional coefficients and the geometry of the rotor. The references of the different stations of the stage and the conventions associated to the triangle of velocity are given in Fig. 1.

Some restrictive hypotheses are required to derive the different expressions. It will be shown that the final expression is accurate enough to account for the dominant physics of the flow:

— steady flow of an inviscid ideal gas
— superposition of one-dimensional axisymmetric flow of thickness dr along the span
— no variation of the rotational speed (axial geometry)
— no density variation across the stage (pressure ratio close to unity)

The flow and loading coefficient thus simplifies as

$$\psi = \frac{\Delta h_i}{U^2} \quad \text{and} \quad \phi = \frac{C_{m1}}{U} \tag{1}$$

The definition of a nondimensional static pressure drop is required.[2]

$$\Delta P^* = \frac{2(P_2 - P_1)}{\rho U^2} \tag{2}$$

---

[2]This definition is equivalent to the usual traction coefficient found in the literature dedicated to propeller.
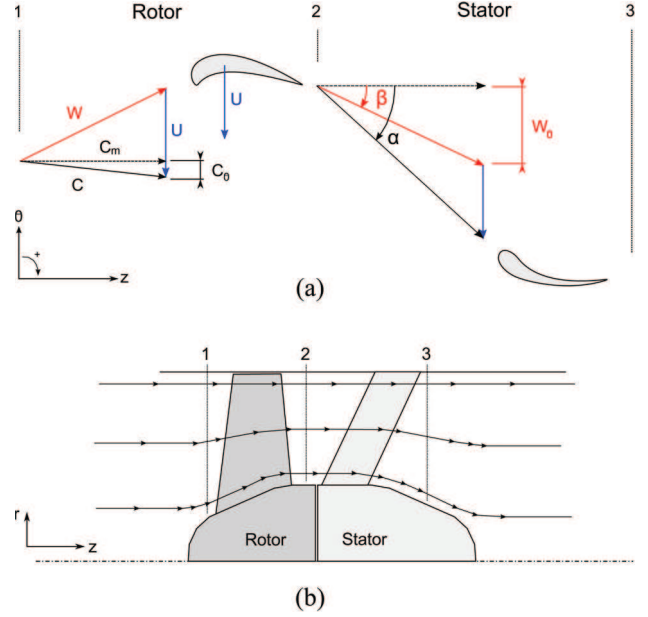

Fig. 1 Conventions and references: (**a**) triangle of velocities and (**b**) stations of a conventional stage

2.3 Derivation at a Given Radial Position. Applying Euler's theorem, the definition of ψ gives

$$\psi = \frac{(U + C_{m2} \tan \beta_2) - (C_{m1} \tan \alpha_1)}{U}$$

Introducing the average velocity ratio $k = (C_{m2}/C_{m1})$, the expression becomes

$$\psi = 1 + n\phi, \quad \text{with} \quad n = (k \tan \beta_2 - \tan \alpha_1) \tag{3}$$

Also, the momentum equation in incompressible and inviscid flows gives

$$U\Delta C_\theta = \frac{1}{\rho}(P_2 - P_1) + \frac{1}{2}\left(C_2^2 - C_1^2\right) \tag{4}$$

A decomposition of the velocities, with the definition of ΔP^* gives a second-order polynom function of ϕ

$$\Delta P^* = a\phi^2 + b\phi + 1 \tag{5}$$

with

$$\begin{cases} a = -[k^2(1 + \tan^2 \beta_2) - (1 + \tan^2 \alpha_1)] \\ b = -2 \tan \alpha_1 \end{cases} \tag{6}$$

Equation (5) thus formalizes the evolution of the pressure drop due to the work exchange and the possible contraction of the meridional channel.

It is stated for strictness that the coefficients n, a, and b are not completely independent of ϕ since either k or the deviation of the flow can directly or indirectly (for example, through the evolution of the Reynolds number) be affected by this coefficient. But this influence is neglected, and the above evolutions are treated as purely linear and quadratic.

2.4 Integration of Radial Evolution. The relations (3) and (5) are not unknown from the literature (mainly the first one

presented in Refs. [17,18] or mentioned in Ref. [4]), but rarely integrated along the span. The strict integration is generally out of the reach of analytical methods and requires a numerical integration (see Ref. [19] for instance). A formulation that includes the radial evolution of the flow is reachable, under certain conditions together with the definition of the adequate reference radius. This requires two additional hypotheses:

— entropy, stagnation enthalpy, and tangential momentum conserved along the radius (free vortex hypothesis: $rC_\theta = cste$)
— curvature in the meridional plane neglected

These hypotheses are clearly restrictive since the "free vortex design" is not a generality. If implemented, it is naive to hope the exact observation of the free vortex flow, because of secondary flows and end-wall boundary layers. But in that context, it can be shown that C_m is constant along the blade span, which greatly eases the integration. The mechanical power exchanged with the flow is

$$\dot{W} = \int_{r_h}^{r_s} d\dot{W}(r) = \int_{r_h}^{r_s} \Delta h_i(r) \cdot d\dot{m}$$

where r_h and r_s are, respectively, the hub and shroud radius of the machine.[3] According to Eq. (3), the definitions of ψ and ϕ and the expression of the mass-flow

$$\dot{W} = \int_{r_h}^{r_s} U(r)[U(r) + n(r)C_{m1}] \cdot \rho C_{m1} 2\pi r dr$$

which is decomposed in

$$\dot{W} = 2\pi\rho C_{m1}\omega^2 \int_{r_h}^{r_s} r^3 dr + 2\pi\rho C_{m1}^2 \omega \int_{r_h}^{r_s} n(r)r^2 dr \quad (7)$$

We define the reference radius as the quadratic mean of the hub and shroud radii

$$\hat{r} = \sqrt{\frac{r_s^2 + r_h^2}{2}} \quad (8)$$

The hatted formalism is used when the radius-dependant quantities are expressed at this reference radius (for example, $\hat{U} = \hat{r}\omega$). Introducing κ_n

$$\kappa_n = \frac{2\hat{r}}{(r_h^2 - r_s^2)} \int_{r_h}^{r_s} \frac{n(r)}{\hat{n}}\left(\frac{r}{\hat{r}}\right)^2 dr \quad (9)$$

Equation (7) reduces to a simple formulation

$$\dot{W} = \dot{m}\hat{U}^2 + \kappa_n \hat{n}\dot{m}C_{m1}\hat{U}$$

which finally gives a new linear evolution

$$\hat{\psi} = 1 + \hat{n}\kappa_n\hat{\phi} \quad (10)$$

It is actually the expression of Eq. (3) at the reference radius, with a correction of the slope κ_n due to the radial integration. The values of both $\hat{n}$ and κ_n can be easily computed from a given geometry, supported by the adequate deviation model. A similar derivation, based on the definition of a mean pressure drop, gives

$$\Delta\hat{P}^* = \hat{a}\kappa_a\hat{\phi}^2 + \hat{b}\kappa_b\hat{\phi} + 1 \quad (11)$$

Fig. 2 Trajectories in the diagrams: (a) generic trends and (b) decomposition of the operating modes

with

$$\begin{cases} \kappa_a = \dfrac{2\hat{r}}{(r_h^2 - r_s^2)} \displaystyle\int_{r_h}^{r_s} \dfrac{a(r)}{\hat{a}}\left(\dfrac{r}{\hat{r}}\right) dr \\ \kappa_b = \dfrac{2\hat{r}}{(r_h^2 - r_s^2)} \displaystyle\int_{r_h}^{r_s} \dfrac{b(r)}{\hat{b}}\left(\dfrac{r}{\hat{r}}\right)^2 dr \end{cases} \quad (12)$$

Once integrated, $\hat{\psi}(\hat{\phi})$ is still linear, $\Delta\hat{P}^*(\hat{\phi})$ is still parabolic. Those trajectories are obviously geometry-dependant. A generic plot is proposed in Fig. 2(a). At the boundary between the quadrants, two specific values of the global flow coefficient are defined. $\hat{\phi}_p$ (subscripted "p" for: power inversion) marks the inversion of the sign of $\hat{\psi}$, which expresses the passage from a fan-like functioning to a turbine-like functioning. The inversion of the sign of $\Delta\hat{P}^*$, which informs that the thrust becomes negative, occurs at $\hat{\phi}_t$ (subscripted "t" for: thrust inversion).[4]

---

[3]If there is an inlet to outlet variation of radius at hub or shroud because of a contraction of the meridional channel, the use of the rotor outlet radius is recommended (the inlet swirl is generally small, and the sine of this angle is considered at the inlet plane; the error of neglecting the meridional curvature is thus imputed on small quantities, which minimizes the global error).
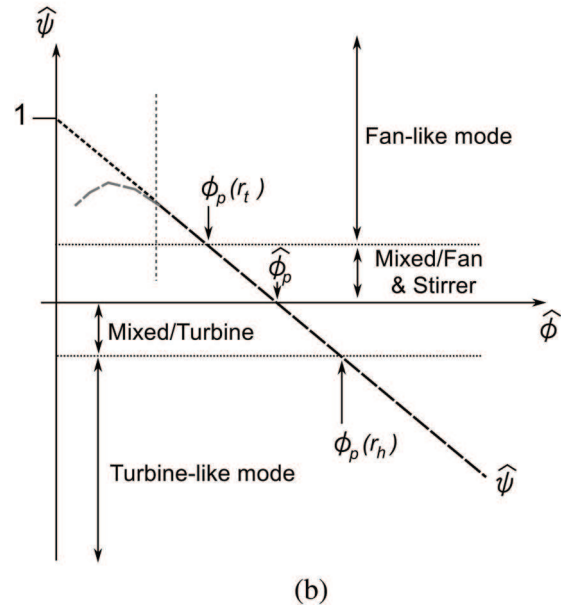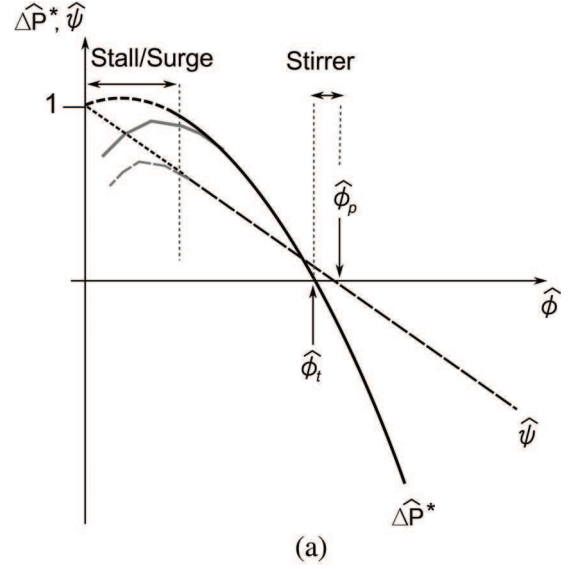
[4]In an inviscid process, it might be observed that $\hat{\phi}_p < \hat{\phi}_t$. But the model does not account for the contribution of losses to the pressure drop. Thus, it will be found that $\hat{\phi}_p > \hat{\phi}_t$. The different operating regimes can thus be identified: for $\hat{\phi} < \hat{\phi}_t$ the usual fan mode, for $\hat{\phi}_t < \hat{\phi} < \hat{\phi}_p$ the stirrer mode, and for $\hat{\phi} > \hat{\phi}_p$ the turbine mode.

For the low values of the flow coefficient, unstable functioning is expected due to stall/surge phenomena. Those phenomena are also out of the reach of such a simple description as the one derived here (here illustrated by the expected drop of the characteristic coefficients).

The generic topology of the characteristic lines for the global coefficients of Fig. 2(a) has been observed in Refs. [11,12] and to a lesser extend in Ref. [18]. This theoretical basis is now analyzed, in order to formulate some expectations concerning the progressive evolution along the operating line.

2.5 Theoretical Expectation of the Flow Topology in the Boundary Region Between the Quadrants.

A more local description of the flow is necessary to detail the generic flow at the boundary region between two quadrants. Let's focus on the transition from fan to turbine. From a global point of view, the limit between these two modes is reached at $\hat{\phi} = \hat{\phi}_p$ and $\hat{\psi} = 0$, with

$$\hat{\phi}_p = -\frac{1}{\kappa_n(k \tan \hat{\beta}_2 - \tan \hat{\alpha}_1)} \qquad (13)$$

This limit obviously depends on the angles of the flow at $\hat{r}$, and on the three-dimensional evolution of the geometry (κ_n). From a local point of view, this limit changes along the blade span. For a given radius, Eq. (3) applies. The local value of the limit between the two operating modes slightly differs from the global one,

$$\phi_p(r) = -\frac{1}{k \tan \beta_2(r) - \tan \alpha_1(r)} \qquad (14)$$

Also, the radial evolution of the local flow coefficient $\phi(r)$ is derived from the value of the reference flow coefficient ($\hat{\phi}$)

$$\phi(r) = \frac{\hat{r}}{r} \hat{\phi} \qquad (15)$$

As a consequence, the nature of the operation can change along the blade span, depending on the local value of $\phi(r)$ compared with the local limit $\phi_p(r)$. Such a mixed configuration can be observed whichever the quadrant considered and not exclusively in free-windmilling. An illustration of the associated composition of velocities is proposed in Fig. 3.

More specifically, for conventional designs of low-speed fans, the inlet swirl can be neglected, and the camber of the blades is
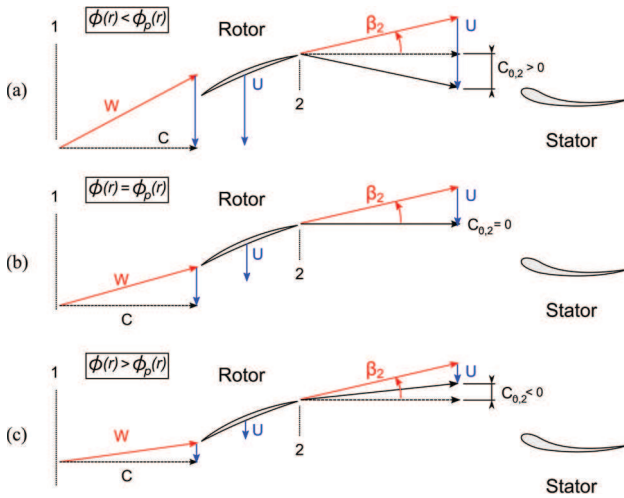
small; β_2 is generally negative all along the blade span. β_2 is more negative at tip than at hub because of the radial evolution of the rotational speed. According to Eq. (13), it is assumed that a typical fan geometry is such that $\phi_p(r_s) < \hat{\phi} < \phi_p(r_h)$. A progressive transition toward turbine operating mode thus has the following consequences on the local topology of the flow (see Fig. 2(b)):

— For $\hat{\phi} \in [0, (r_s/\hat{r})\phi_p(r_s)]$, the operating point is in the conventional fan quadrant; some work is transmitted to the flow all along the blade span (Fig. 4(a)).

— For $\hat{\phi} \in [(r_s/\hat{r})\phi_p(r_s), \hat{\phi}_p]$, the operating point is still in the conventional fan quadrant, but for the upper section of the blade $\phi(r) > \phi_p(r)$. It is thus a mixed configuration: the fan operation is contaminated by local turbine functioning, initiated at the tip of the blades. The neutral radius along the blade span is quoted r_p. As the contamination grows with the increase of $\hat{\phi}$, the net work transmitted to the flow decreases, and no longer compensate the losses. The stirrer operating mode is then observed (Fig. 4(b)).

— For $\hat{\phi} = \hat{\phi}_p$, there is an exact match between extraction and transmission contribution to the work exchange. The overall power exchange is null; the fan operates in free-windmilling. The neutral radius r_p is close to $\hat{r}$ (depending on the value of κ_n, i.e., the twisting of the blade). Some negative incidence is observed within the turbine region (Fig. 3). Speaking of viscous flows, separation of the boundary layer at the lower surface of the blades is expected. The spanwise evolution of the solidity (pitch-to-chord ratio, see Ref. [20]) and the interaction with the tip vortex flows
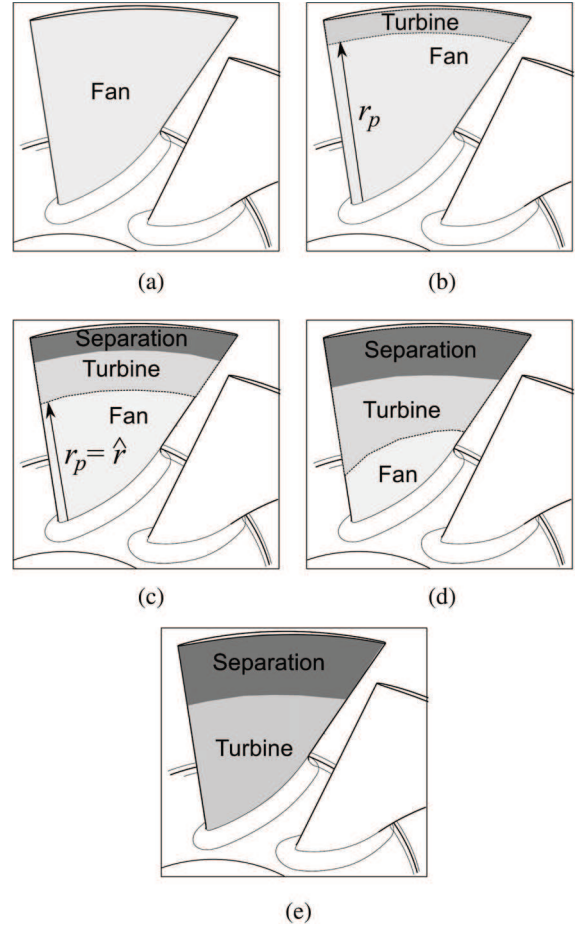

Fig. 4 Illustration of the local operating mode along the blade span, for different values of the operating flow coefficient: (*a*) $0 < \hat{\phi} < (r_s/\hat{r})\phi_p(r_s)$, (*b*) $(r_s/\hat{r})\phi_p(r_s) < \hat{\phi} < \hat{\phi}_p$, (*c*) $\hat{\phi} = \hat{\phi}_p$, (*d*) $(r_s/\hat{r})\phi_p(r_h) > \hat{\phi} > \hat{\phi}_p$, and (*e*) $\hat{\phi} > (r_s/\hat{r})\phi_p(r_h)$

Fig. 3 Possible local composition of velocities (without inlet swirl) along the span: (*a*) fan-like, (*b*) neutral, and (*c*) turbine-like

Table 1 Characteristics of the fans

	Fan 1	Fan 2
IGV (deg)	0, 10, and 20	—
diam/diam$_{\text{ref}}$	1	1.23
Design speed (rpm)	$\approx$12,000	$\approx$12,000
Design flow coefficient	0.58	0.3
Design pressure ratio	1.02	1.039

involve a special exposure of the upper section of the blades to this phenomenon (Fig. 4(*c*)).

— For $\hat{\phi} \in [\hat{\phi}_p, (r_h/\hat{r})\phi_p(r_h)]$, the contamination of the turbine mode is such that the net transfer of work is now negative, and the machine recovers some energy from the flow. But this energy recovery is far from efficient, since the lower part of the blade still transfers work to the flow. The machine is now in the turbine quadrant, still with a mixed operating configuration along the blade span (Fig. 4(*d*)).

— For $\hat{\phi} > (r_h/\hat{r})\phi_p(r_h)$, the operating mode is turbine-like all along the blade span. The shifting of quadrant is completed. The machine recovers some work, but the strong negative incidence is likely to provoke massive separation of the flow (Fig. 4(*e*)). The energy recovery induces some negative swirl at the outlet of the rotor, if the inlet flow is purely axial. This might be a problem for the downstream elements (such as the stator, if any is present). Massive separation inside the stator has been reported in many studies ([12,14,16], cite7-2 and Ref. [7]).

3 Experimental Approach

Some experiments were conducted in order to check the validity of the theoretical expectations. Two low-speed fans stages (rotor + stator) dedicated to aircraft air systems (characteristics in Table 1) are considered. The first geometry (fan 1) is used for global characterization of the operating point and quantification of the power recovery/transfer from/to the flow. An optional inlet guide vane (IGV) device can produce some inlet swirl. The second geometry (fan 2) is used for local measurement inside the flow. Both fans are coupled with an electrical engine (synchronous machine with permanent magnet), which is used not only to drive the rotor in the fan mode, but also to set the loading of the shaft in the turbine mode. It is thus possible to explore the two quadrants of the flow coefficient maps. The two experimental setups are quite similar and can be decomposed in three main parts: the first one is used for the mass flow measurement, the second one is the test section in which the fan is located, and the last one is used for the flow generation, if needed (turbine mode). The two experiments illustrated in Fig. 5 are successively detailed.

3.1 Experimental Setup of Fan 1. The experiment dedicated to fan 1 is operated in an industrial environment. The mass-flow measurement is performed through an orifice-plate system, designed and instrumented according to the norm ISO 5801 [21]. An IGV with three angular positions can be installed at the inlet of the test section. This test section is reversible (i.e., its orientation in the flow can be inverted). As a consequence, a large number of operating configurations are possible, including reverse flow configurations. When needed, two additional fans generate the main flow in the test section. The air can be either sucked or blown.
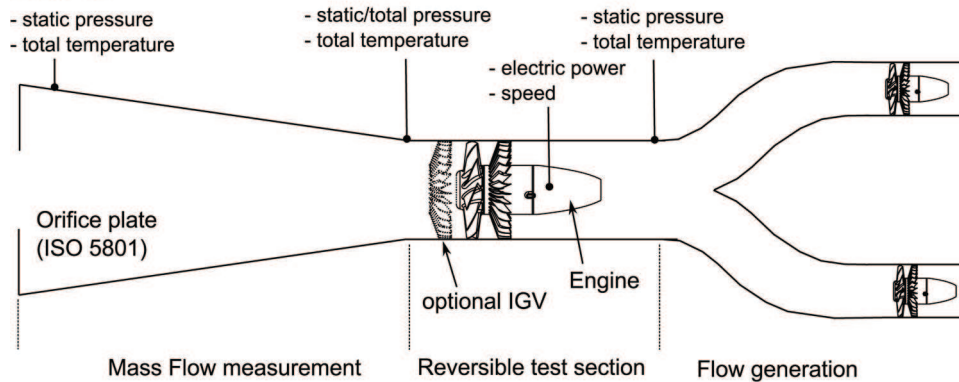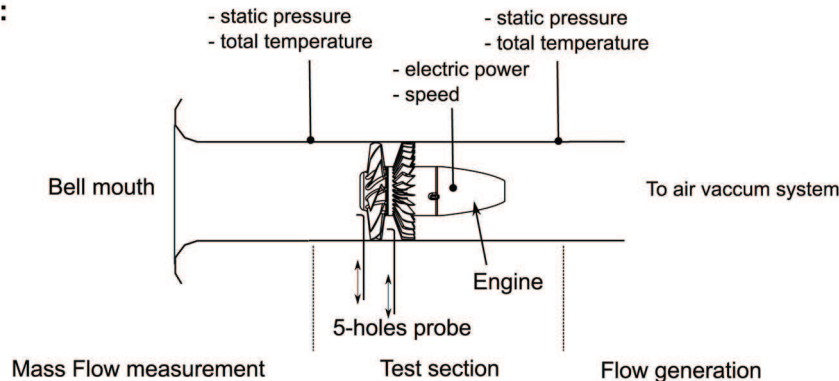

Fig. 5 Illustration of the experimental setup for the two fans: (*a*) fan 1 and (*b*) fan 2

Three piezometric chambers connected to differential sensors (Druck sensors, ± 100 mbar, basic accuracy 0.1% FS) give access to the static pressure downstream of the orifice plate, at the inlet and outlet of the test section. Platinum probes (A-Class PT100, basic accuracy ±0.2 °C) give the total temperature at the same location. A Prandtl probe gives the total pressure at the inlet of the test section. The temperature rise (or drop) is very small since the pressure ratio of the stage is very close to unity. The power transferred (or recovered) to (from) the flow is thus difficult to measure accurately by the use of total temperature evolution. A better accuracy is reached through the measurement of the electric power plugged in the engine. A VOLTECH PM 3000A multimeter (basic accuracy of 0.05% rdg + 0.05% rng on each voltage and current channel) measures the individual electric power of the three phases of the engine, together with the frequency of the rotor (±0.1%). The characterization of the electric engine allows the proper correction of the power measurement to account for the magnetic losses, mechanical losses, and Joule losses. The data acquisition is performed by a 20 channel multiplexer 34901A connected to an Agilent 34970A data acquisition device (60 channel/s scanning, resolution of 22 bits). Once the steady-state of the fan is reached, the measurements are recorded during 50 s, at a sampling frequency of 1 Hz. The very low dispersion of the measurements during the recording time shows an excellent operating stability of the fan, including in severe windmilling conditions.

The fan mapping is performed with the test section in reversed configuration (different calibrated orifice plates change the loading of the fan) through the recoding of speed-lines. The turbine mapping is performed with the test section in direct configuration, in which the flow is sucked by the two high pressure (HP) fans; the recoding is organized along some isoloading lines (constant resistive loading of the electrical engine), for different flow conditions.

3.2 Experimental Setup of Fan 2. The experiment of the fan 2 is conducted in a research lab. The flow measurement is performed through a calibrated bell-mouth. The test section, possibly reversible, is connected to the air vacuum system of the lab when a flow generation is needed. The instrumentation is quite similar to that of the fan 1. The sensor used for pressure measurements (including five-hole probes) are Rosemoundt 3051 pressure transmitters, with an accuracy of ±0.15% FS. The electric power is measured with VOLTECH PM 3000A multimeter (basic accuracy of 0.05% rdg + 0.05% rng on each voltage and current channel).

In windmilling conditions, radial probing of the velocity and pressure is carried-out by the use of five-hole probes, 1 mm upstream the leading edge of the rotor at hub and 1 mm downstream the rotor trailing edge at hub. For each of the 20 positions along the radius, the flow pressures are recorded, and postprocessed with the calibration map of the probe. Some preliminary tests have identified a low frequency fluctuation ($\approx 10^{-1}$ Hz) of the flow, whose magnitude strongly depends on the radial position of the probe (very intense at the tip of the blades). The exact origin of this fluctuation is not fully understood, and out of the reach of the present steady metrology. It is conjecturally imputed to the complex flow topology, which involves massive flow separation. A recording time long enough to reach the statistic convergence of the mean value is thus necessary at each location of the radial probing, to avoid phase lag between the different measurements. This recoding time is set at 30 s. The data acquisition is performed with a composite NI cDAQ-9172 device equipped with NI 9215 modules for current measurements (analogic/digital converter (ADC) 16 bits, up to 200 kech/s), NI 9203 for voltage measurements (ADC 16 bits, up to 100 kech/s), and NI 9211 for temperature measurements (ADC 24 bits, up to 14 ech/s/ch with noise rejection). For steady operating points, 1000 samples are recorded during 0.1 s. A dispersion and repeatability analysis has been conducted (also for longer recoding times), which shows an excellent stability of the fan operation, such as the one observed for the fan 1.

The turbine mapping is performed by setting the vacuum intensity, for which the resistive loading of the engine is progressively

increased. The radial probing is recorded for two fixed values of the flow coefficient: the free-windmilling value ($\hat{\phi} = \hat{\phi}_p = 0.7$) and a second one inside the load-controlled windmilling quadrant ($\hat{\phi} = \hat{\phi}_l = 0.75$) for which two speed lines overlap (at 4600 rpm and 8000 rpm). It is thus possible to compare two different operating points, with the same value of the flow coefficient.

3.3 Uncertainties. The uncertainties of the different sensors are composed by the use of the usual derivative propagation method. The final uncertainty accounts for the accuracy of the sensors and the repeatability ability of the bench. It is plotted in figures as error bars. For the local measurements with the five-hole probes, the low frequency previously discussed introduces a dispersion which is greater than the expected uncertainty. The variance of this dispersion will thus be used for the error bars.

4 Presentation of the Results and Discussion

4.1 Operating Line in the $\hat{\psi} - \hat{\phi}$ Diagram. The results presented in Figs. 6 and 7 show the operating evolution recorded for both the fans in the $\hat{\psi} - \hat{\phi}$ map, with and without the presence of the IGV.

The operating range tested is much wider for the fan 1 than for the fan 2, because of limitations in power generation/dissipation in the experiment of fan 2. The continuous evolution from the
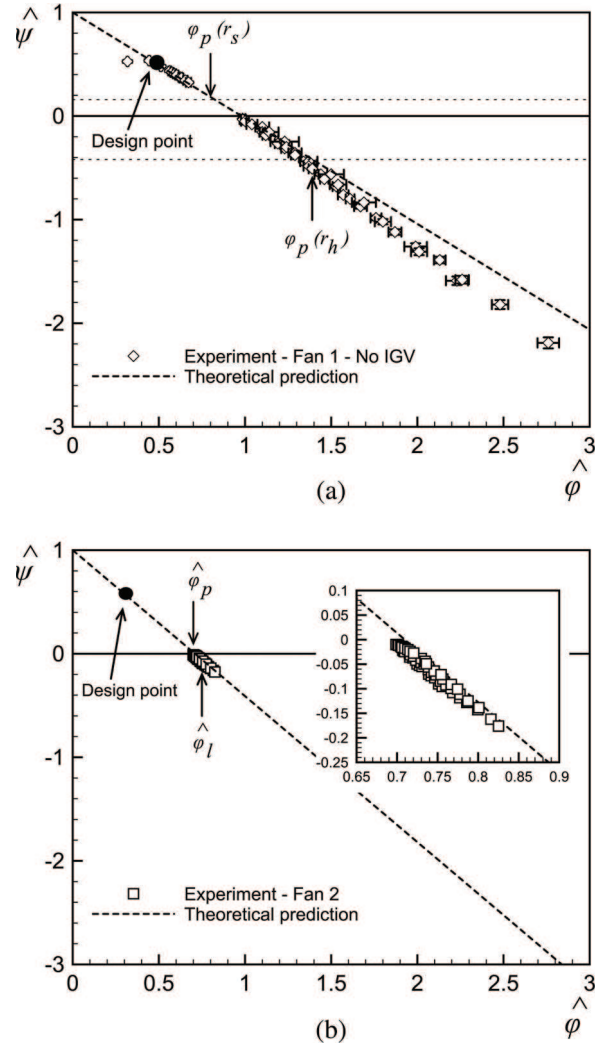

Fig. 6 Experimental results for the two fans without preswirl, compared with the theoretical expectation: (a) fan 1 and (b) fan 2
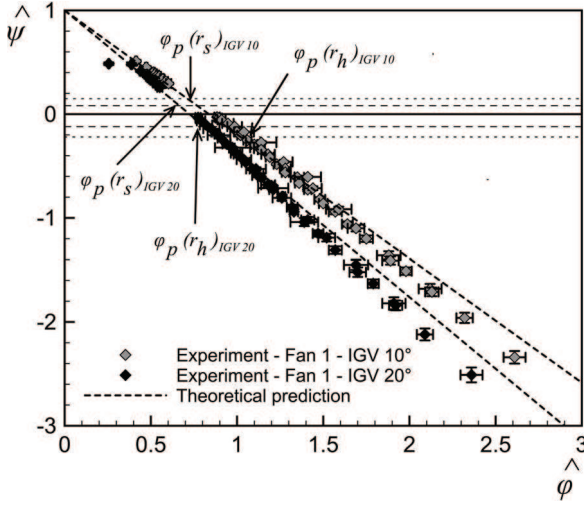
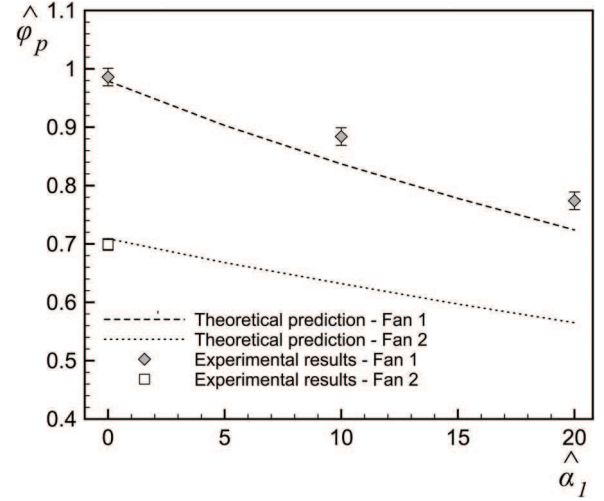**Fig. 7 Experimental results for the fan 1 with preswirl, compared with the theoretical expectation**

Fig. 8 Comparison between the theoretical prediction of $\hat{\phi}_p$ as a function of the inlet swirl and the experimental results for the two fans

fan-like operating mode toward turbine-like operating mode is observed for all the cases, as expected from Eq. (10). The trajectory is linear, except for the greatest values of flow coefficient. The boundary region defined by $\phi_p(r_s)$ and $\phi_p(r_h)$ inside which the spanwise coexistence of turbine and compressor functioning is expected is also represented in Figs. 6(a), and 7. The operating trajectory crosses this boundary region without noteworthy alterations.

The theoretical prediction is plotted, based on Eq. (10). The coefficients $\hat{n}$ and κ_n can be computed using only the geometric definition of the rotor blade (Eq. (9)). To provide a pragmatic account of viscous effects, deviation can be included in the computation in a straightforward way by using Carter's relation (recommended in Ref. [7]). In all cases, the model does not require any fitting operation. The agreement between this prediction and the experimental results is good for the two fans. The relative error does not exceed 20% for the fan 1 whichever the IGV configuration is, and generally drops below 7% for $\hat{\phi} < \phi_p(r_h)$. A partial correlation exists between this error and the level of negative incidence on the rotor blades (cross-correlation coefficient = 0.71): large negative incidence can be at the origin of flow separation which cannot be predicted by the model. The presence of the preswirl moderates this incidence for a given value of $\hat{\phi}$ because of velocity composition. This explains why the agreement between model and results is better in Fig. 7 than in Fig. 6(a). Anyway the question of the accuracy of Carter's rule for such important values of the flow coefficient naturally rises.

From a practical point of view, it is interesting to observe that $\hat{\phi}_p$, which is representative of a free-windmilling operation, is located in a low-error region of the theoretical trajectory. When needed, it can be usefully predicted with fair accuracy as shown in Fig. 8 or can be extrapolated from results obtained in fan operating-mode.

4.2 Operating Line in the $\Delta \hat{P}^* - \hat{\phi}$ Diagram. The evolution of the stage measured and reported in the $\Delta \hat{P}^* - \hat{\phi}$ map is more complex to compare to the theoretical expectation, for many reasons. First, the contribution of the rotor has not been isolated on the fan 1; only the global stage pressure drop has been measured. Second, Eq. (11) does only account for the pressure rise/drop consequent to some work transfer to/from the flow, and to the evolution of the meridional channel. Actually the losses due to viscous effects will generate an additional pressure drop. The contribution of each of theses processes is interesting to analyze anyway. In incompressible flows, the following decomposition is possible:

$$\Delta P^* = \Delta P^*|_{\text{work}} + \Delta P^*|_{\text{losses}}$$

Equation (11) is supposed to predict $\Delta P^*|_{\text{work}}$. On the fan 2, the isolated contribution of the rotor to the pressure drop is measured. The results are presented in Fig. 9(a). Compared with the theoretical evolution, the trend is correct, but inaccurate because of the losses. An attempt to extract the contribution of the losses from the experimental data is proposed. The approach is quite similar to the one depicted in Ref. [7]. It focuses on the data collected in free-windmilling. In that regime, the overall work exchange is generally neglected; the loss mechanism is the only contribution to the pressure drop and can be identified. In reality, a residual torque exists on the shaft because of mechanical and electromagnetic losses (internal to the electrical engine). The work exchange associated to this residual torque is subtracted from the pressure drop, and the loss contribution is isolated. It is converted into a loss coefficient, $\xi = (\Delta P / P_{i1})$, which is evaluated as a function of the reduced mass-flow $\dot{m}_r = (\dot{m}\sqrt{rT_{i1}}/A_1P_{i1})$.

The observed evolution is in agreement with the one reported in Ref. [7], either in the trend, or in the amount of losses generated by the isolated rotor ($\xi < 0.01$). A second-order fit is recommended in Ref. [7]. Such a model is extracted and used to estimate the losses in load-controlled windmilling. This contribution is subtracted to the measured pressure drop coefficient. The contribution of the work exchange is thus isolated. The corrected data are reported in Fig. 9(a) and collapse fairly well on the predicted evolution. This validation is not strict since it can be opposed that the losses are estimated for a fixed value of the flow coefficient (namely at $\hat{\phi} = \hat{\phi}_p$), and then transposed to greater values (losses are expected to increase with the flow coefficient). But it is fair enough to give some credit to Eq. (11) as a good representation of the pressure drop due to work exchange.

The results concerning the fan 1 are plotted in Fig. 10 for two configurations of preswirl. It has been formerly stated that this pressure drop accounts for the whole stage, including the diffuser. It is quoted $\Delta \hat{P}^*_{1-3}$ and can be hardly correlated to the theoretical prediction. But some elements are worth being reported such as the good matching in fan operation. Near the design point, the losses are presumably small compared with the work exchange. The latter is then the dominant contributor to the pressure rise, and its modeling gives a good representation of the actual behavior.

A decomposition such as the one applied on fan 2 is hardly possible on fan 1, since the losses are now generated by the IGV, the rotor, and the diffuser. Anyway, the results obtained for both the fan-like and turbine-like operating modes collapse on the same trend for a fixed preswirl configuration. This enforces the relevance of ΔP^* as a rightful similitude parameter and suggests a
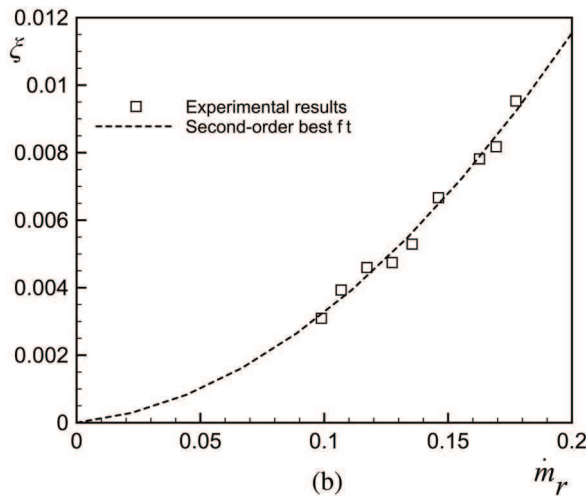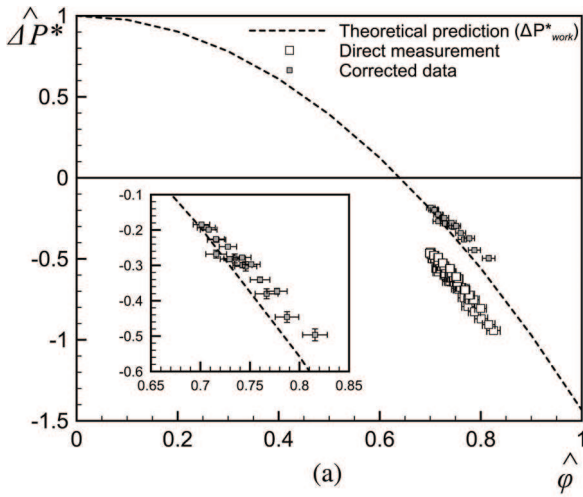
Fig. 9 Analysis of fan 2. (*a*) Evolution of the pressure-drop coefficient as a function of the flow coefficient, for direct measurement and corrected data, compared with the theoretical expectation. (*b*) Estimation of the pressure loss coefficient, as a function of the reduced mass-flow.
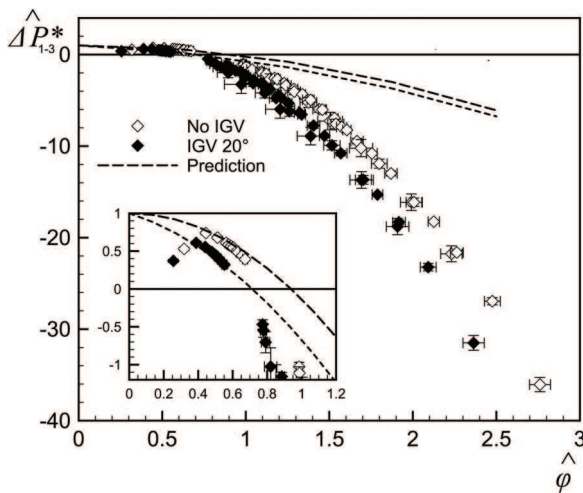

Fig. 10 Overall pressure drop coefficient as a function of the flow coefficient for the fan 1, for two different IGV configurations

strong correlation between $\Delta P^*|_{\text{losses}}$ and $\hat{\phi}$. The use of this formalism is thus recommended for the losses.

4.3 Local Topology of the Flow. The local probing of the three operating points $(\hat{\phi} = \hat{\phi}_\text{p}, N = 8000\,\text{rpm}; \hat{\phi} = \hat{\phi}_\text{l}, N = 4600\,\text{rpm}; \text{and } N = 8000\,\text{rpm}, \text{see Fig. } 6(b))$ is used for a local validation of Eq. (3); the local values of $\phi(r)$ and $\psi(r)$ are post-processed. The local coefficient $n(r) = (\psi(r) - 1/\phi(r))$ is calculated and compared to the theoretical computation from the geometry (Carter's rules are once again applied). The results are presented in Fig. 11(*a*). The experimental results are in fair agreement with the geometric evaluation of $n(r)$, especially near the hub, at $\hat{\phi}_\text{p}$. A degradation of this agreement is observed at $\hat{\phi}_\text{l}$. An increase of the casing region affected by the low-frequency fluctuations recorded during the experiments is also observed. The predictive accuracy of the model is strongly influenced by that of the deviation model. The Carter's rule prediction is thus compared with the measurements (Fig. 11(*b*)). The deviation model underpredicts the deviation of the flow, which is understandable since it is out of its validity range. The value is rather constant on the two lower thirds of the blade span, around 10 deg. This is consistent with the results reported from a compressor cascade at highly negative incidence (see Ref. [9]). The upper third of the blade experiences a more complex topology. This region is supposedly affected by massive separation of the boundary layer, and by tip-clearance secondary flows.
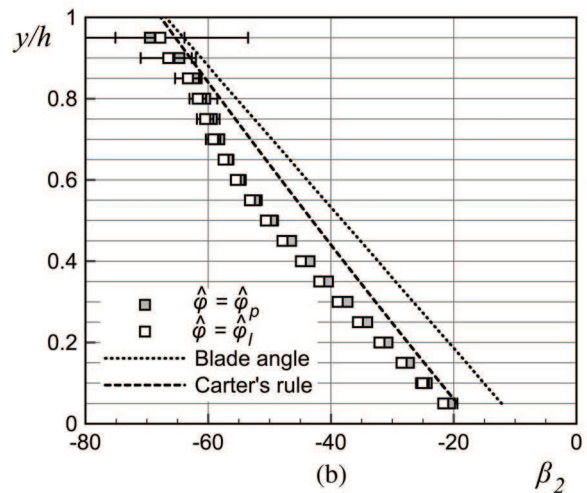

(a)
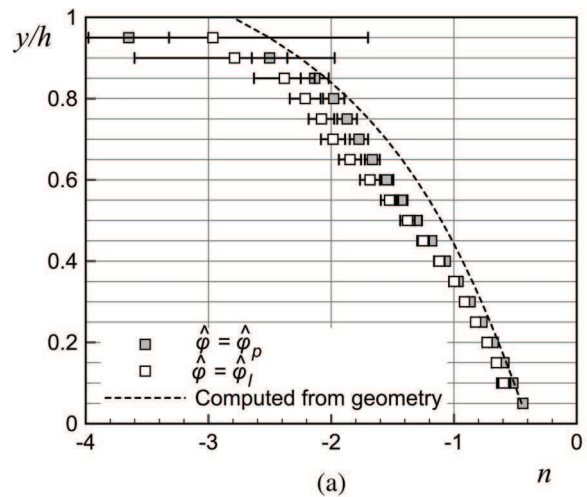

(b)

Fig. 11 Distribution along the blade span compared with expectation predicted from geometry, for $\hat{\phi}_\text{p}$ and $\hat{\phi}_\text{l}$. (*a*) Local ψ-to-ϕ gradient. (*b*) Relative flow angle at the outlet of the rotor.

Anyway the model is representative enough to conduct some generic analysis about the work exchange along the blade span, for mixed configurations. More specifically, an examination of setting of the neural radius r_p is proposed.

The local variation of the total enthalpy across the rotor (reduced by the square of the reference blade speed) is predicted along the span of the blade (Fig. 12). The overall flow coefficient is gradually increased, from free-windmilling to load-controlled windmilling (Fig. 12(a)). The prediction illustrates the expected response of r_p to the overall flow coefficient increase: a shifting toward the hub as the fan gets farther inside the turbine operating mode. But another characteristic of the flow also interferes with this topology: a uniform velocity distribution has been supposed at the inlet of the rotor to ease the integration, which is compromised in viscous flow. A distortion of the flow is thus simulated in the near-wall region, with an increased intensity (the parameter δ indicates the ratio of the channel affected by the distortion). This distortion is unity-averaged so that it does not affect the overall mass-flow; its influence in free-windmilling operation is illustrated in Fig. 12(b). The turbine operating-mode usually found in the upper part of the blade is greatly affected by the deficit of inlet velocity. As a consequence, the balance canceling compressor and turbine contributions is modified, and r_p is displaced downward. Near the casing, a new region of compressor or stirrer operation may appear.
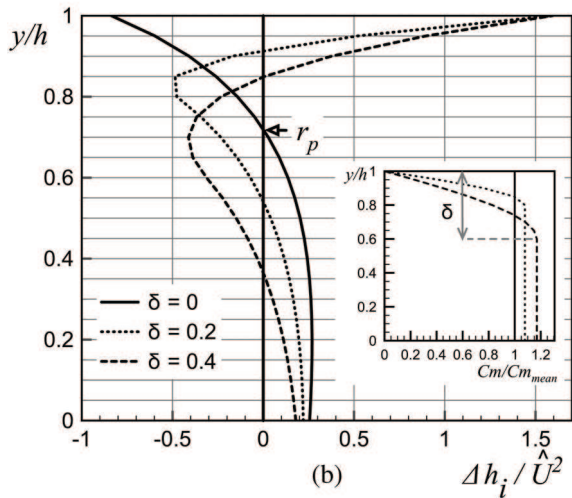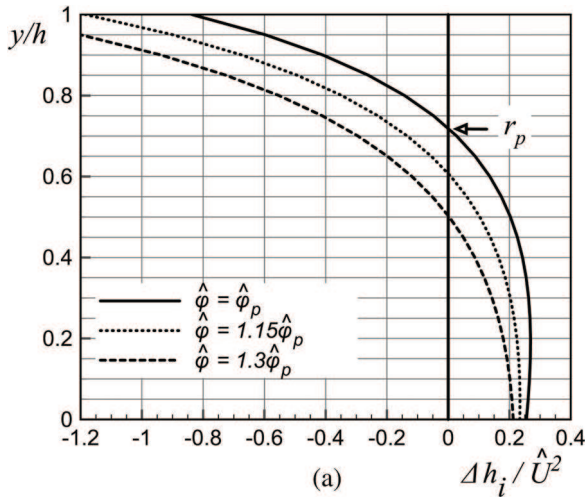
Fig. 12 Local prediction of the local enthalpy variation along the blade span; evolution of the neutral radius r_p. (a) Increase of the flow coefficient for a uniform inlet velocity distribution. (b) Distortion of the inlet velocity distribution for $\hat{\phi} = \hat{\phi}_p$.
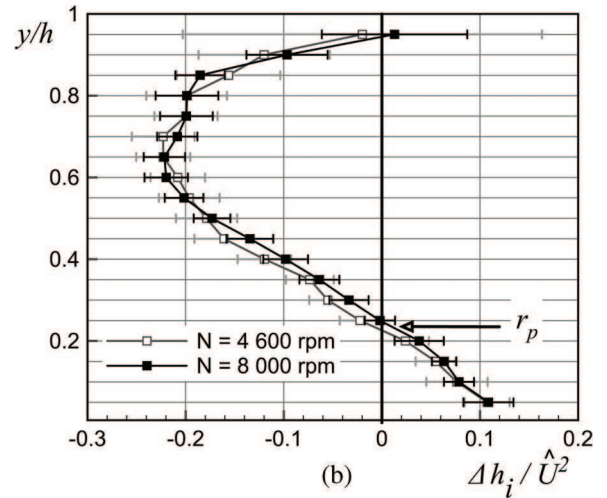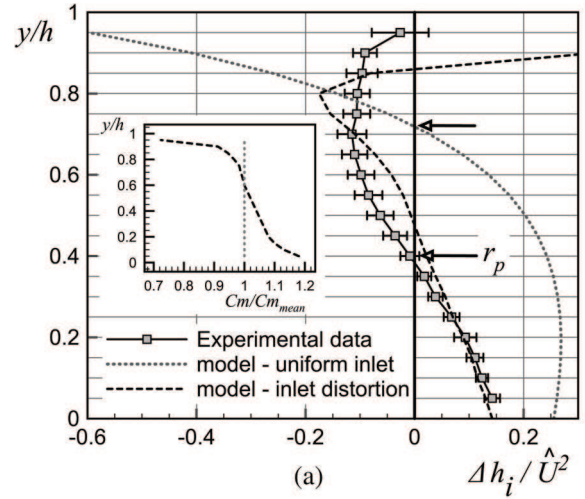
Fig. 13 Distribution of the dimensionless total enthalpy change along the blade span. The predicted and effective neutral radius positions are quoted. (a) $\hat{\phi} = \hat{\phi}_p$. (b) $\hat{\phi} = \hat{\phi}_l$.

Summarizing, for a given blade geometry, the radial distribution of the operating modes depends not only of the flow coefficient, but also of the inlet velocity profile. This has been experimentally observed, as show in Fig. 13, where the enthalpy variation is evaluated by the use of the probing of the inlet and outlet flow angles. Figure 13(a) shows the results in free-windmilling operation, in comparison with two predictions: with and without the influence of the inlet distortion recorded for the experimental facility.[5] Its influence on the local topology is striking and well captured by the model. Also, the co-existance of turbine-mode and compressor mode canceling each other is clearly measured.

At $\hat{\phi} = \hat{\phi}_l$, the regime shifts toward load-controlled windmilling operation. The co-existence of the two operating modes is still observed, but the extraction of work is now the dominant operating mode; r_p is decreased. A trend toward the appearance of another layer of compressor-like operation at the tip of the blade is observed. The results obtained for the two different rotational speed collapse on the same trend. It demonstrates that, for a given geometry and a given inlet distortion, the local topology of the flow is a function of the global flow coefficient. The results presented in Ref. [7] also show such a property even if it is not commented in the text: the neutral radius is the same for the three

---

[5]This distortion is mainly due to viscous effect at the shroud, and to the presence of the hub cap.

mass-flows considered in the paper, which is understandable since the simulations of the paper were all performed at $\hat{\phi}_p$, i.e., in free-windmilling.

4.4 Local Analysis of the Losses. A local treatment of the different contributions to the pressure drop is attempted. By the use of the local momentum equation (see Eq. (4)), it is possible to evaluate the contribution of the work exchange, which has been probed. This contribution is added to the inlet distribution of total pressure. The result is compared to the outlet probing of the total pressure (Fig. 14(a)). The difference between the two curves represents the losses, which are also plotted in Fig. 14(b). On the lower part of the blade, the main contributor to the total pressure rise is the work exchange, but it decreases along the span. The losses are small in that section, but increase gradually along the blade. A limit is reached when those two contributions are equal: a local stirrer mode is then observed on a small portion of the blade. Above this region, some work is extracted from the flow. The losses increase drastically in the local turbine mode and become the main contributor to the pressure drop. A final evolution of the work exchange back to positive values is observed, but the uncertainties do not allow to certify the presence of another local stirrer mode on the upper part of the blade. Massive separation of the boundary layer is expected in that region, which probably explains the high level of losses.

Considering the loss coefficient itself (ξ), a detailed analysis of the loss distribution is difficult because of the composition of the

uncertainties (three different measurement devices are used) and the fluctuation. The alternative definition aforementioned ($\Delta P^*|_{losses}$) is also plotted, which should be correlated to the flow coefficient value. There again, the uncertainties do not allow to draw definitive conclusions, but some trends appear.

5 Outlook on Potential Application of the Model

5.1 System Level Predictions. The fact that the windmilling of fans is almost exclusively studied inside its system shows how much system-dependant this phenomenon is. For an aero-engine, it is understood that the free-wheeling rotational speed cannot be predicted without an accurate estimation of the overall losses. Those losses will define the mass-flow, which in turn will define the freewheeling rotational speed [5]. However, another approach is possible, in which the rotor is treated separately from the other elements of the system, as within the model proposed herein. Any other static element of the system, such as the outlet guide vane, can be considered as a loss generator with its own "permeability." In this approach, two coupling parameters are identified. The first one is the distortion of the inlet velocity distribution. On large fans with short inlet ducts and purely axial supply, this might not be significant. But for low Reynolds number applications, with long ducting and complex integration, it might be of some importance. The second parameter is the shaft loading, which determines the loading coefficient. Those two parameters will set both the global and local performance. In the example of the windmill of aero-engines, the shaft loading is such that the loading coefficient is null. It fixes the operating flow coefficient at $\hat{\phi}_p$ and also the local topology if the inlet distortion is neglected. To predict the rotational speed, the knowledge of the mass flow is still required and will depend on the overall permeability (losses, outlet conditions, etc.). But this approach gives some flexibility: an alteration of the permeability can be easily handled, since the ratio of the mass-flow to the rotational speed is still constant ($\hat{\phi} = \hat{\phi}_p$). This is also interesting in the prospect of changing the shaft loading, for energy recovery or other applications. Finally, this special treatment of the rotor avoids the pragmatic (but questionable) amalgam made between the contributions (losses and work) to the pressure drop/rise, generally found in the literature dealing with free-windmilling.

5.2 Potential of Fans for Energy Recovery. It is obvious that the potential of energy recovery of actual fans is poor. Both the large negative incidence and the mixed-operation regions damage this potential. The use of an IGV enhances the energy recovery, but at the detriment of the fan operating mode performance. If possible, the inversion of the flow direction is an efficient solution [11,16] since the velocity triangle is much more adapted to turbine operation: the diffuser acts like a turbine nozzle. But this pragmatic solution may not be applied due to integration constraints. This issue requires the design of a rotor fit for the dual operation, which still needs to be formalized. A model such as the one derived in the present work can be an efficient tool to define the outlines of such a nonconventional design.

6 Conclusion

The present work is a contribution to the understanding of low-speed fans in windmilling operation. The evolution of the rotor flow is described by the use of theoretical and experimental data. Some characteristic trajectories have been identified in the usual diagrams of the fan, which synthesize the operating possibilities of a given geometry. The local topology of the flow is described along those trajectories; the gradual evolution of the compressor operating mode toward the turbine operating mode is detailed. A generic analysis of the situation is proposed. It is shown that

— the local co-existence of compressor and turbine operating modes is observed near the boundary region between the
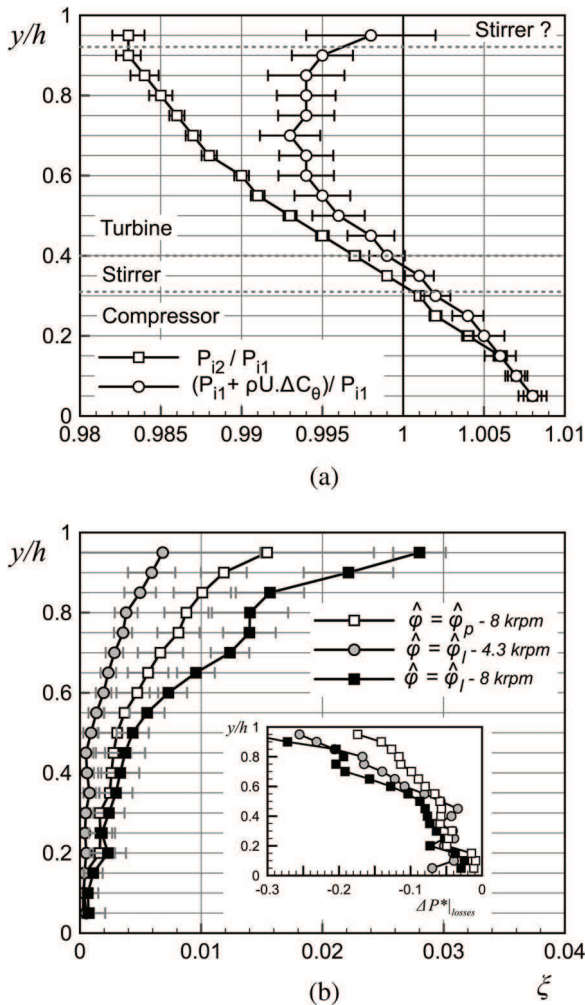

Fig. 14 Spanwise evolution of the losses. (a) Contributions to the total pressure ratio at $\hat{\phi} = \hat{\phi}_p$. (b) Loss coefficients (main figure: ξ, subfigure: $\sim\Delta P^*|_{losses}$).

two quadrants and not exclusively in free-windmilling conditions. This mix-functioning region can be predicted from the geometric definition of the fan
— for conventional fans, the contamination of the compressor operating mode by the turbine operating mode is initiated in the upper region of the blades and progresses downward as the flow coefficient increases
— without radial distortion of the inlet conditions, the local distribution of the operating-modes along a given blade geometry and the location of the neutral position only depend on the value of the flow coefficient
— the presence of a radial distortion at the inlet can have a strong influence on the local distribution between the modes; the position of the neutral radius can be modified, and additional operating modes can be observed
— the global and local identification of the losses should be isolated from the work exchange in order to establish clear correlations

The theoretical model presented here is physically consistent, even if its validity is limited by the complexity of viscous flows. The predictability is strongly dependant of the model used for the flow deviation at the trailing edge of the blades. The recommendation of Carter's rule is reinforced in the present work, even if the definition of a model adapted to strong negative incidence could further enhance the results.

A strong correlation between the contribution of the losses to the nondimensional pressure drop and the flow coefficient is suspected, if not formally demonstrated. It is envisaged as a continuity of this work.

Finally, the strong dependence of the windmilling operation to systems aspects is assessed. The present study proposes a special treatment of the rotor, since it is the only element that actually exchanges energy with the flow. It could be argued that a coupling exists between the overall permeability of the system and the operation of the rotor. Such a coupling could be, for example, the modification of the flow incidence on the stator, when the regime of the rotor is modified. Two cases are considered: if the modification of the regime is operated with the same flow coefficient, the variation of the flow angle at the outlet of the rotor will be marginal, and so will be the alteration of the loss process. If the modification involves a variation of flow coefficient, some interaction could be expected. But this interaction is expected to be small with reasonable confidence: the negative incidence on the stator of conventional fans is such that additional variations should not change drastically the huge amount of losses generated.

Nomenclature

a = second-order coefficient of the flow-to-pressure evolution
b = first-order coefficient of the flow-to-pressure evolution
C = absolute velocity (m s^{-1})
h = height of the blade (m)
k = average velocity ratio
$\dot{m}$ = mass-flow rate (kg s^{-1})
$\dot{m}_r$ = reduced mass-flow rate
n = flow-to-loading coefficient gradient
N = rotational speed (rpm)
P = pressure (Pa)
r = radius (m)
T = temperature (K)
U = blade velocity (m s^{-1})
W = relative velocity (m s^{-1})
$\dot{W}$ = power (W)
Δh = enthalpy variation per mass unit (J kg^{-1})
ΔP^* = pressure drop coefficient

Greek Symbols

α = flow angle in the absolute frame

β = flow angle in the relative frame
δ = characteristic relative length of the inlet distortion
ξ = pressure loss coefficient
κ = spanwise integration coefficient
ρ = fluid density (kg m^{-3})
ψ = loading coefficient
ϕ = flow coefficient
ω = angular rotation speed (s^{-1})

Subscripts

a = relative to the coefficient a
b = relative to the coefficient b
h = relative to hub
i = total state
m = meridional component
n = relative to the coefficient n
p = at power inversion
s = relative to shroud
t = at thrust inversion
0 = stage inlet
1 = rotor inlet
2 = stator inlet
3 = stator outlet
θ = tangential component

Alteration

$\hat{\cdot}$ = relative to the reference radius

References

[1] Daggett, D. L., Brown, S. T., and Kawai, R. T., 2003, *Ultra-Efficient Engine Diameter Study*, NASA Glenn Research Center, Cleveland, OH.
[2] Walsh, P. P., and Fletcher, P., 2004, *Gas Turbine Performance*, Wiley, Boston.
[3] von Groll, G., and Ewins, D. J., 2000, "On the Dynamics of Windmilling in Aero-Engines," 7th IMechE International Conference on Vibrations in Rotating Machinery, Nottingham, UK, Sept. 12–14, Paper No. C576/024/2000, pp. 721–738.
[4] Riegler, C., Bauer, M., and Kurzke, J., 2001, "Some Aspects of Modeling Compressor Behavior in Gas Turbine Performance Calculations," ASME J. Turbomach., **123**(2), pp. 372–378.
[5] Zachos, P. K., 2013, "Modelling and Analysis of Turbofan Engines Under Windmilling Conditions," J. Propul. Power, **29**(4), pp. 882–890.
[6] Pilet, J., Lecordix, J. L., Garcia-Rosa, N., Barènes, R., and Lavergne, G., 2011, "Towards a Fully Coupled Component Zooming Approach in Engine Performance Simulation," ASME Paper No. GT2011-46320.
[7] Prasad, D., and Lord, W. K., 2010, "Internal Losses and Flow Behavior of a Turbofan Stage at Windmill," ASME J. Turbomach., **132**(3), p. 031007.
[8] Goto, T., Kato, D., Ohta, Y., and Outa, E., 2014, "Unsteady Flow Structure in an Axial Compressor at Windmill Condition," ASME Paper No. GT2014-25609.
[9] Zachos, P. K., Grech, N., Charnley, B., Pachidis, V., and Singh, R., 2011, "Experimental and Numerical Investigation of a Compressor Cascade at Highly Negative Incidence," Eng. Appl. Comput. Fluid Dyn., **5**(1), pp. 26–36.
[10] Rosa, N. G., Dufour, G., Barènes, R., and Lavergne, G., 2015, "Experimental Analysis of the Global Performance and the Flow Through a High-Bypass Turbofan in Windmilling Conditions," ASME J. Turbomach., **137**(5), p. 051001.
[11] Rosero, J. A., Ortega, J. A., Aldabas, E., and Romeral, L. A. R. L., 2007, "Moving Towards a More Electric Aircraft," IEEE Aerosp. Electron. Syst. Mag., **22**(3), pp. 3–9.
[12] Turner, R. C., and Sparkes, D. W., 1963, "Paper 6: Complete Characteristics for a Single-Stage Axial-Flow Fan," Proc. Inst. Mech. Eng., **178**(9), pp. 14–27.
[13] Gill, A., von Backström, T. W., and Harms, T. M., 2007, "Fundamentals of Four-Quadrant Axial Flow Compressor Maps," Proc. Inst. Mech. Eng., Part A, **221**(7), pp. 1001–1010.
[14] Gill, A., von Backström, T. W., and Harms, T. M., 2012, "Reverse Flow Turbine-Like Operation of an Axial Flow Compressor," ASME Paper No. GT2012-68783.
[15] Gill, A., Von Backström, T. W., and Harms, T. M., 2014, "Flow Fields in an Axial Flow Compressor During Four-Quadrant Operation," ASME J. Turbomach., **136**(6), p. 061007.
[16] Zachos, P. K., Aslanidou, I., Pachidis, V., and Singh, R., 2011, "A Sub-Idle Compressor Characteristic Generation Method With Enhanced Physical Background," ASME J. Eng. Gas Turbines Power, **133**(8), p. 081702.
[17] Courty Audren, S. K., Carbonneau, X., Binder, N., and Challas, F., 2013, "Potential of Power Recovery of a Subsonic Axial Fan in Windmilling Operation," 10th European Turbomachinery Conference, Lappeenranta, Finland, Apr. 15–19.

[18] McKenzie, A. B., 1997, *Axial Flow Fans and Compressors: Aerodynamic Design and Performance*, Ashgate, Farnham, UK.

[19] Lakshminarayana, B., 1996, *Fluid Dynamics and Heat Transfers of Turbomachinery*, Wiley Interscience, New York.

[20] Cumpsty, N. A., 1989, *Compressor Aerodynamics*, Longman Scientific & Technical, Essex, UK.

[21] Illana, E., Grech, N., Zachos, P. K., and Pachidis, V., 2013, "Axial Compressor Aerodynamics Under Sub-Idle Conditions," ASME Paper No. GT2013-94368.

[22] NF EN ISO 5801 Janvier, 2009, *Ventilateurs industriels—Essais aérauliques sur circuits normalizes*, AFNOR, pp. 31–54.

[23] Dixon, S. L., and Hall, C. A., 2010, *Fluid Mechanics and Thermodynamics of Turbomachinery*, 6th ed., Butterworth-Heinemann, Boston.